Competing Magnetic Interactions in the Antiferromagnetic Topological Insulator $MnBi_2Te_4$

Bing Li,[1,2] J.-Q. Yan,[3,*] D. M. Pajerowski,[3] Elijah Gordon,[1] A.-M. Nedić◉,[1,2] Y. Sizyuk,[1] Liqin Ke,[1] P. P. Orth◉,[1,2] D. Vaknin◉,[1,2] and R. J. McQueeney[1,2,†]

[1]*Ames Laboratory, Ames, Iowa 50011, USA*
[2]*Department of Physics and Astronomy, Iowa State University, Ames, Iowa 50011, USA*
[3]*Oak Ridge National Laboratory, Oak Ridge, Tennessee 37831, USA*

The antiferromagnetic (AFM) compound $MnBi_2Te_4$ is suggested to be the first realization of an AFM topological insulator. We report on inelastic neutron scattering studies of the magnetic interactions in $MnBi_2Te_4$ that possess ferromagnetic triangular layers with AFM interlayer coupling. The spin waves display a large spin gap and pairwise exchange interactions within the triangular layer are long ranged and frustrated by large next-nearest neighbor AFM exchange. The degree of frustration suggests proximity to a variety of magnetic phases, potentially including skyrmion phases, which could be accessed in chemically tuned compounds or upon the application of symmetry-breaking fields.

The breaking of time-reversal symmetry by the introduction of magnetism in topological materials is key to unlocking unique topologically protected transport phenomena [1]. For example, the quantum anomalous Hall effect has been demonstrated at low temperatures by inducing bulk ferromagnetism (FM) through the substitution of dilute magnetic ions, such as Cr or V, into $(Bi, Sb)_2(Se, Te)_3$ topological insulators [2–4]. While this is an incredibly important discovery, the disorder and inhomogeneity associated with these dilute FM systems present an obstacle to delivering quantum topological transport at routinely accessible temperatures. An alternate route to access these phenomena is to develop a new class of stoichiometric magnetic topological materials. $MnBi_2Te_4$ may be the first example of a stoichiometric antiferromagnetic topological insulator (AFTI) [5–11]. AFTI are predicted to provide a platform for novel topological phases, such as quantum anomalous Hall insulators, axion insulators, or Weyl semimetals [12]. The symmetry, strength, and anisotropy of the magnetic interactions in AFTIs are important factors that control access to these quantum topological states.

$MnBi_2Te_4$ is a closely related structural variant of the tetradymite topological insulators, such as Bi_2Te_3. Whereas the teteradymite structure consists of stacked Te-Bi-Te-Bi-Te triangular (quintuple) layers, $MnBi_2Te_4$ consists of Te-Bi-Te-Mn-Te-Bi-Te septuple layers. The electronic topology of inverted Bi-Te bands found in the tetradymites is similar in $MnBi_2Te_4$ while the Mn triangular layers host large $S = 5/2$ magnetic moments. The AFM ordering of Mn moments consists of FM triangular layers with AFM interlayer coupling, referred to as A-type AFM order, with moments pointing perpendicular to the layers [5,11]. The

A-type structure provides access to novel topological phases via thin film growth with odd (time-reversal symmetry breaking) or even (Z_2 invariant) septuple layers [10,13]. In addition, relatively weak-field metamagnetic transitions allow access to canted, spin-flopped, or fully polarized magnetic structures [8,9,11]. This flexibility of the magnetic structure has been utilized to demonstrate the QAH effect [14].

In this Letter, inelastic neutron scattering (INS) measurements on $MnBi_2Te_4$ reveal its Ising-like nature, surprisingly strong interlayer exchange interactions, and large lifetime broadening. We find that the next-nearest neighbor AFM interaction (J_2) competes with nearest-neighbor FM interaction (J_1) within the triangular layer, placing the system close to the classical stability limit for intralayer FM correlations $|J_2/J_1| < 1/3$ [15,16]. In addition, we find that longer-range interactions up to at least the fourth neighbor are necessary to fully describe the intralayer spin dynamics. These experimental observations are supported by first-principles (DFT + U) calculations of the magnetic interactions which are long-ranged and frustrated at correlation strengths of $U \approx 4$–5 eV. Our classical Monte Carlo simulations show that the system is susceptible to forming long-period magnetic structures. This may allow, for example, the Bi-Te layers containing topological fermions to be subjected to a variety of helimagnetic or topological skyrmionic structures [17] under suitable perturbations, such as chemical substitution or applied magnetic fields.

INS measurements on powder samples of $MnBi_2Te_4$ ($T_N = 24$ K) were performed on the Cold Neutron Chopper Spectrometer (CNCS) at the Spallation Neutron Source at Oak Ridge National Laboratory using incident neutron energies of $E_i = 3.3$ and 12 meV. The intensities
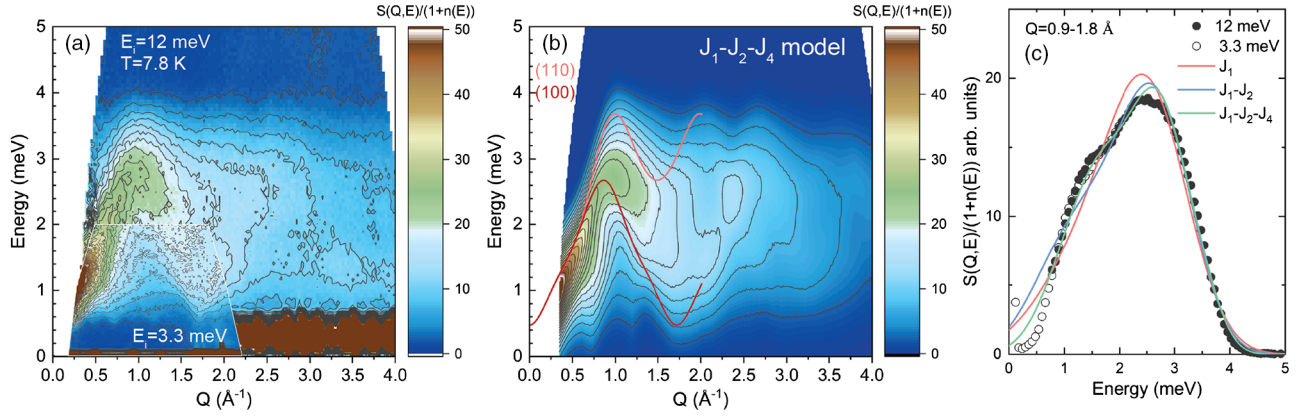
FIG. 1. (a) Inelastic neutron scattering intensities of both the $E_i = 12$ and $E_i = 3.3$ meV data plotted versus Q and E from a powder sample of MnBi$_2$Te$_4$ in the ordered AFM phase at $T = 7.8$ K. (b) Results of the J_1-J_2-J_4 Heisenberg model calculations of the powder-averaged INS intensity. Pink and red lines are the dispersion in the (110) and (100) directions, respectively. (c) Comparison of different Heisenberg models to the experimental data including intralayer interactions up to nearest neighbor, (red line), next-nearest neighbor (blue line), and fourth-nearest neighbor (green line).

are plotted as $S(Q,E)/[1 + n(E)]$, where Q is the momentum transfer, E is the energy transfer, and $n(E) = [\exp(E/k_B T) - 1]^{-1}$ is the Bose population factor. This intensity is proportional to the imaginary part of the dynamical susceptibility times the square of the magnetic form factor, $f^2(Q)\chi''(Q,E)$. Other data treatment details are described in the Supplemental Material [18].

Figure 1(a) shows the Q and E dependencies of the $E_i = 3.3$ meV INS data superimposed on the 12 meV data measured in the AFM phase at $T = 7.8$ K. The data show dispersing spin wave excitations that emanate from $Q \approx 0$, reach a maximum energy of $E \approx 3.5$ meV near the Brillouin zone boundary of the triangular layer at $Q \approx 1$ Å^{-1}, and return to a finite energy due to a spin gap near the magnetic/nuclear (1,0,L) zone centers at $Q \approx 1.7$ Å^{-1}. The signal weakens for larger Q due to the magnetic form factor. The magnetic spectral features are very broad and the 3.3 and 12 meV datasets are nearly indistinguishable despite the sizable difference in instrumental energy resolution [full-width-at-half-maximum (FWHM) of 0.15 and 0.7 meV, respectively]. This provides evidence for strong intrinsic sources of line broadening, such as magnon-phonon and/or magnon-electron coupling. Surprisingly, the INS features are qualitatively similar to the FM-TI (Bi$_{0.95}$Mn$_{0.05}$)$_2$Te$_3$ [19], where dilute concentrations of Mn are expected to substitute randomly into Bi triangular layers.

Figures 2(a)–2(c) show the spin gap structure in more detail. Despite the heavy broadening of the higher energy modes, Fig. 2(a) and constant energy Q cuts in Fig. 2(b) find sharp dispersion minima at momenta of $(0,0,3/2)$, $(0,0,9/2)$, and $(0,0,15/2)$, corresponding to A-type AFM zone centers. This observation suggests that interlayer interactions are not negligible, which is surprising given the large spacing of 13.6 Å between Mn layers. An energy

cut at the dispersion minimum at $(0,0,9/2)$ ($Q = 0.7$ Å^{-1}) in Fig. 2(c1) indicates a spin gap with an onset of $\Delta \approx 0.5$ meV consistent with sizable uniaxial magnetic anisotropy.

The quantitative details of the magnetic interactions become more apparent based on fitting the data to a local-moment Heisenberg model,

$$H = -\sum_{ij_\parallel} J_{ij}\mathbf{S}_i \cdot \mathbf{S}_j - J_c \sum_{\langle ij \rangle_\perp} \mathbf{S}_i \cdot \mathbf{S}_j - D\sum_i S_{i,z}^2, \quad (1)$$

where $J_{ij} \equiv J_l$ describe pairwise interactions between the lth neighbors within a single triangular layer, J_c corresponds to an AFM nearest-neighbor (NN) interlayer coupling, and $D > 0$ is the uniaxial anisotropy. Here $J > 0$ corresponds to FM coupling. As we describe below, the sharpness of interlayer modes at the gap edge and the broad, high energy intralayer modes necessitate a stepwise approach to determine all model parameters.

Analysis of the magnetization data provides preliminary estimates of the interlayer interaction J_c and uniaxial anisotropy D parameters (J_c-D model). The magnetization, measured at $T = 2$ K on single-crystal specimens shown in Fig. 2(e), reveals spin-flop and saturation fields $H_{SF} = 3.4$ T and $H_{sat}^c = 7.9$ T with $H\|c$ and $H_{sat}^{ab} = 10.3$ T with $H\|ab$, consistent with previous reports [8,9,11]. Within the Heisenberg model and starting from A-type order with moments along c, these critical fields are given by the expressions $g\mu_B H_{SF} = 2S\sqrt{D(6|J_c| - D)}$, $g\mu_B H_{sat}^c = 2S(6|J_c| - D)$, and $g\mu_B H_{sat}^{ab} = 2S(6|J_c| + D)$ (where $g \approx 2$ and $S \approx 5/2$) and provide a range of values for $SD \approx 0.07$–0.1 meV and $-SJ_c \approx 0.08$–0.09 meV. The magnetization data provide an estimate for $\Delta = 2S\sqrt{D(6|J_c| + D)} = 0.4$–0.5 meV that is consistent with the INS data in Fig. 2(c1).
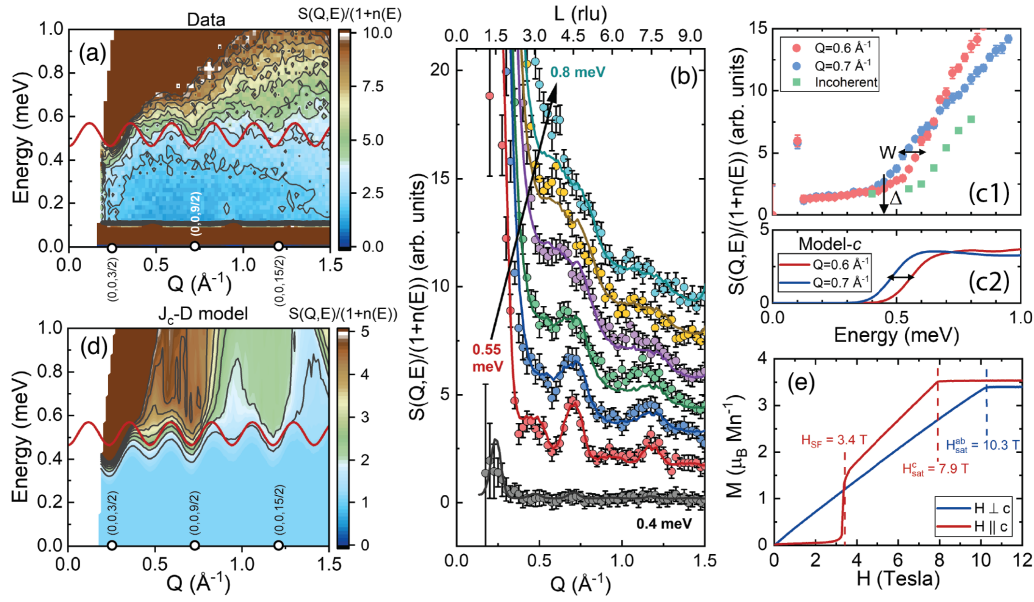
FIG. 2. (a) Inelastic neutron scattering intensities of $MnBi_2Te_4$ measured at $T = 7.8$ K focused on the low energy gap edge with $E_i = 3.3$ meV. (b) Several constant energy Q cuts at the gap edge from the data (circles) and from Model cD (lines). Plots are vertically offset for clarity. (c1) Low energy magnetic energy spectrum showing the spin gap (Δ) near $(0, 0, 9/2)$ ($Q = 0.7$ Å^{-1}, blue circles) and an estimate of the bandwidth (W) using a cut near the interlayer AFM zone boundary ($Q = 0.6$ Å^{-1}, red circles). Green squares are estimates of the incoherent background originating from intralayer spin wave modes. (c2) Same cuts as in (c1) obtained from the J_c-D model. (d) Numerical calculations of the INS intensity from the J_c-D model. In (a) and (d), the red line shows the dispersion of spin wave modes along c from the J_c-D model. (e) Magnetization data from a single crystal of $MnBi_2Te_4$ highlighting spin-flop and saturation fields.

We also analyze the J_c-D model parameters by comparing the gap edge INS data to calculations of the powder-averaged spin wave intensities following the procedure outlined in Ref. [20]. We assume resolution-limited features (FWHM = 0.15 meV) and fix SJ_1 to a nominal value since the energies are too low to effectively fit the intralayer exchange parameters. We then vary SJ_c and SD and compare the calculated spin wave intensities to a series of constant-energy Q-cuts from 0.4–0.8 meV, as shown in Fig. 2(b). Much better agreement with the data is obtained by the addition of incoherent background contributions that presumably originate from the broad, intralayer excitations described below. The resulting χ^2 goodness-of-fit displays a rather shallow minimum that does not allow precise determination of SD and SJ_c (see Fig. S4 in the Supplemental Material [18]) and deviates somewhat from the values determined from the magnetization data.

Within the shallow minimum in χ^2, a representative set of parameters can be ascertained from INS data by considering the spin gap and the bandwidth of interlayer excitations (W) shown in Fig. 2(c1). The bandwidth is determined by the energy at the AFM zone boundary at $Q = 0.6$ Å^{-1}, where $W = 6S|J_c| + 2SD - \Delta \approx 0.1$ meV. Δ and W provide rough estimates of $SD \approx 0.12$ and $SJ_c \approx -0.055$ meV that sit within the minimum in χ^2 and Figs. 2(a)–2(d) shows these parameters provide a good representation of the gap edge data.

We now turn to the determination of the intralayer model parameters. This fitting was performed by fixing the J_c-D model values and sampling intralayer J_l values over a regular mesh and calculating the powder averaged magnetic scattering. The calculated spectrum was convoluted with the instrumental resolution function and compared to the measured magnetic spectrum of the $E_i = 12$ meV data summed over the momentum range from $Q = 0.8$–1.9 Å^{-1}. A satisfactory accounting of all features in the magnetic spectrum requires the introduction of intralayer pairwise exchange interactions up to the 4th neighbor.

For NN coupling (J_1) only, the best-fit model spectrum consists of a single sharp peak near the top of the spin wave band with $SJ_1 = 0.26$ meV. Reasonable fitting to the J_1 model requires the introduction of a substantial Gaussian lifetime broadening FWHM of $\Gamma = 1.5$ meV to the calculated spectra. Figure 1(c) shows that the J_1 model is clearly an unsatisfactory description of the experimental spectrum. The introduction of a frustrating AFM next-nearest-neighbor (NNN) interaction (J_2) improves the fit by shifting magnetic spectral weight from high to low energies. As Fig. 1(c) shows, the resulting fit to the J_1-J_2 model with optimized values of $SJ_1 = 0.31$ and $SJ_2 = -0.06$ meV is better, but even this model requires sizable damping of 1.1 meV. Neither the J_1 nor the J_1-J_2 models capture the broad, low energy peak between 1–1.5 meV which led us to consider even longer-range interactions.

TABLE I. Heisenberg model parameters obtained from low energy INS data (J_c-D model), high energy INS data (J_1, J_1-J_2, and J_1-J_2-J_4 models), and DFT $+ U +$ SOC calculations. The broadening parameter (Γ) is also provided. All values are in meV.

	SJ_1	SJ_2	SJ_4	SJ_c	SD	Γ	χ^2
J_c-D	0.23	$\cdots$	$\cdots$	-0.055	0.12	0.1	$\cdots$
J_1	0.26(1)	$\cdots$	$\cdots$	-0.055	0.12	1.5	282
J_1-J_2	0.31(2)	$-0.06(2)$	$\cdots$	-0.055	0.12	1.1	149
J_1-J_2-J_4	0.30(2)	$-0.083(9)$	0.023(8)	-0.055	0.12	0.7	44
DFT	0.81	-0.30	0.13	-0.09	0.15	$\cdots$	$\cdots$

Based on analysis of the spin wave density-of-states (see Supplemental Material [18]), an additional van Hove singularity is introduced to the magnetic spectrum for 4th neighbor interactions (J_4), but not for J_3. This lead us to finally consider the refinement of a J_1-J_2-J_4 model for the intralayer spin dynamics. As shown in Fig. 1(c), this model captures the two-peaked spectrum with optimal values of $SJ_1 = 0.3$, $SJ_2 = -0.083$, and $SJ_4 = 0.023$ meV and $\Gamma = 0.7$ meV. In all models, the value obtained for SJ_1 is consistent with that obtained from single-crystal INS studies of hexagonal MnTe [21], whose structure contains similarly stacked Te-Mn-Te triangular layers. All fitting parameters are reported in Table I.

In all models of the intralayer exchange constants, best fits are obtained when we introduce substantial Gaussian broadening to the calculated spectra beyond the instrumental resolution, suggesting significant lifetime broadening of the intralayer spin waves. Nonetheless, gap edge data representing the interlayer dynamics are very sharp ($\Gamma < 0.15$ meV). This points to the presence of Q- or E-dependent broadening whose complexity prevents simultaneous fitting of high and low resolution data. Single-crystal experiments would be necessary to completely sort out the long-range nature of the interactions along with a complicated damping response.

Our major finding is that competing interactions within the triangular layer are significant ($|J_2/J_1| \approx 0.3$) and come close to the classical instability limit for intralayer FM ground state ($|J_2/J_1| = 1/3$). While the longer-range FM interactions and strong Ising anisotropy will stabilize FM layers, we expect that chemical doping or other perturbation, such as strain, can possibly induce noncollinear phases. To quantify this expectation, we have calculated the magnetic phase diagram (including a magnetic field) using classical Monte Carlo (MC) simulations for a single layer with interactions up to NNN. In Fig. 3(a), we show the low-T phase diagram close to the experimentally found anisotropy value $D/J_1 = 0.4$ as a function of $|J_2/J_1|$ and magnetic field h/J_1 along the z direction. Vertical spiral, skyrmion, and up-up-down-down stripe phases [see Figs. 3(b)–3(d)] appear at larger frustration ratios of $|J_2/J_1| \geq 0.5$. MC simulations also find skyrmion phases appear for smaller anisotropy values $D/J_1 \lesssim 0.1$ at
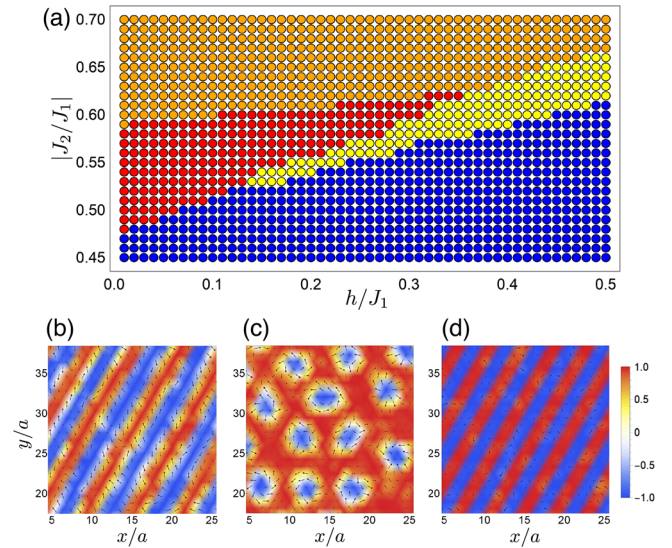

FIG. 3. (a) Low-temperature magnetic phase diagram as a function of $|J_2/J_1|$ and magnetic field h/J_1 for fixed anisotropy $D/J_1 = 0.4$ and temperature $T = 0.08J_1$. Different phases are polarized paramagnet (blue), vertical spiral (red), multi-q (skyrmion) phase (yellow), and up-up-down-down (orange). (b)–(d) Real-space spin configurations of vertical spiral (b), multi-q (skyrmion) crystal (c), and up-up-down-down phases (d). Color denotes S^z component (scale bar shown) and arrows denote the in-plane components (S^x, S^y). Panels show a 20×20 part of the full 52×52 lattice with lattice constant $a = 1$.

$|J_2/J_1| = 0.4$ (see Supplemental Material [18]). This raises the possibility for spiral or skyrmion phases to appear, for example, in Sb-substituted $Mn(Bi, Sb)_2Te_4$, where D is found to be significantly smaller [22].

Recent first-principles electronic structure calculations with $U = 5.34$ eV predict that $|J_2/J_1| < 0.03$ [8,10], which is ten times less than that obtained from our INS data. Here, we extract the Heisenberg parameters by performing an analysis of the energies of six ordered spin states [23] based on DFT $+ U$ calculations [24] including spin-orbit coupling. Figure 4(a) reveals that the DFT results support the presence of strong long-range intralayer interactions at small values of U. Larger values of U suppress long-range interactions. While the DFT $+ U$ generated exchange values are generally larger than the experimental values, the ratios of J_2/J_1 and J_4/J_1 at values of $U \approx$ 4–5 eV are consistent with the INS data. Further details of the computational methods in full can be found in the Supplemental Material [18], which includes Refs. [25–29].

Overall, our findings indicate that AFTI $MnBi_2Te_4$ shows elements of frustration ($|J_2/J_1| \approx 0.3$), Ising anisotropy ($D/J_1 \approx 0.4$), metamagnetism ($|J_c|/D \approx 0.45$), and long-range intralayer exchange interactions ($J_4/J_1 \approx 0.1$). The presence of low-field metamagnetism in $MnBi_2Te_4$ is similar to that found in MX_2 transition metal halide triangular lattice antiferromagnets [30]. Compounds such as $FeCl_2$ [31] and $FeBr_2$ [32] also display
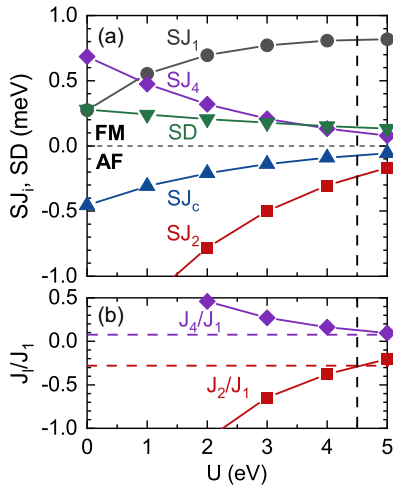
FIG. 4. First-principles calculations of (a) Heisenberg parameters and (b) ratios of key exchange interactions versus U including spin-orbit coupling. In (b), the red and purple horizontal dashed lines correspond to experimental values for J_2/J_1 and J_4/J_1 and the vertical black dashed line shows the best value of $U \approx 4.5$ eV.

strongly competing J_1-J_2 interactions within the triangular layer and can host multi-q magnetic structures [30]. MX_2 compounds have therefore been proposed to host skyrmion phases in applied fields [17]. In $MnBi_2Te_4$, similar frustration could lead to skyrmion phases and may also result in complex spin textures near the sample surface, where magnetic interactions may be modified by strain or surface termination effects. This could explain recent ARPES [33,34] and thin film magnetization data [13] that are not consistent with uniformly FM layers near the surface. Even from our powder samples, we find evidence for strongly $\mathbf{Q}$-dependent broadening, which should be investigated in INS studies of single-crystal samples. Such lifetime broadening could be related to frustration or to coupling between magnetic fluctuations and charge carriers, as inferred from magnetotransport measurements [22].

*yanj@ornl.gov
†mcqueeney@ameslab.gov

[1] Y. Tokura, K. Yasuda, and A. Tsukazaki, Nat. Rev. Phys. 1, 126 (2019).

[2] J. Zhang, C.-Z. Chang, P. Tang, Z. Zhang, X. Feng, K. Li, L.-l. Wang, X. Chen, C. Liu, W. Duan et al., Science 339, 1582 (2013).

[3] C.-Z. Chang, J. Zhang, X. Feng, J. Shen, Z. Zhang, M. Guo, K. Li, Y. Ou, P. Wei, L.-L. Wang et al., Science 340, 167 (2013).

[4] C.-Z. Chang, W. Zhao, D. Y. Kim, H. Zhang, B. A. Assaf, D. Heiman, S.-C. Zhang, C. Liu, M. H. W. Chan, and J. S. Moodera, Nat. Mater. 14, 473 (2015).

[5] S. V. Eremeev, M. M. Otrokov, and E. V. Chulkov, J. Alloys Compd. 709, 172 (2017).

[6] M. M. Otrokov, T. V. Menshchikova, M. G. Vergniory, I. P. Rusinov, A. Y. Vyazovskaya, M. K. Yu, G. Bihlmayer, A. Ernst, P. M. Echenique, A. Arnau et al., 2D Mater. 4, 025082 (2017).

[7] D. Zhang, M. Shi, K. He, D. Xing, H. Zhang, and J. Wang, Phys. Rev. Lett. 122, 206401 (2019).

[8] M. M. Otrokov, I. I. Klimovskikh, H. Bentmann, A. Zeugner, Z. S. Aliev, S. Gass, A. U. B. Wolter, A. V. Koroleva, D. Estyunin, A. M. Shikin et al., Nature (London) 576, 416 (2019).

[9] S. H. Lee, Y. Zhu, Y. Wang, L. Miao, T. Pillsbury, H. Yi, S. Kempinger, J. Hu, C. A. Heikes, P. Quarterman et al., Phys. Rev. Research 1, 012011 (2019).

[10] M. M. Otrokov, I. P. Rusinov, M. Blanco-Rey, M. Hoffmann, A. Y. Vyazovskaya, S. V. Eremeev, A. Ernst, P. M. Echenique, A. Arnau, and E. V. Chulkov, Phys. Rev. Lett. 122, 107202 (2019).

[11] J.-Q. Yan, Q. Zhang, T. Heitmann, Z. Huang, K. Y. Chen, J. G. Cheng, W. Wu, D. Vaknin, B. C. Sales, and R. J. McQueeney, Phys. Rev. Mater. 3, 064202 (2019).

[12] R. S. K. Mong, A. M. Essin, and J. E. Moore, Phys. Rev. B 81, 245209 (2010).

[13] Y. Gong, J. Guo, J. Li, K. Zhu, M. Liao, X. Liu, Q. Zhang, L. Gu, L. Tang, X. Feng et al., Chin. Phys. Lett. 36, 076801 (2019).

[14] Y. Deng, Y. Yu, M.-Z. Shi, J. Wang, X.-H. Chen, and Y. Zhang, Science 367, 895 (2020).

[15] Y. Tanaka and N. Uryu, Prog. Theor. Phys. 55, 1356 (1976).

[16] K. Murao, F. Matsubara, and T. Kudo, J. Phys. Soc. Jpn. 65, 1399 (1996).

[17] A. O. Leonov and M. Mostovoy, Nat. Commun. 6, 8275 (2015).

[18] See Supplemental Material at http://link.aps.org/supplemental/10.1103/PhysRevLett.124.167204 for details of sample preparation, data analysis, and theoretical treatment.

[19] D. Vaknin, D. M. Pajerowski, D. L. Schlagel, K. W. Dennis, and R. J. McQueeney, Phys. Rev. B 99, 220404(R) (2019).

[20] R. J. McQueeney, J. Q. Yan, S. Chang, and J. Ma, Phys. Rev. B 78, 184417 (2008).

[21] W. Szuszkiewicz, E. Dynowska, B. Witkowska, and B. Hennion, Phys. Rev. B 73, 104403 (2006).

[22] J.-Q. Yan, S. Okamoto, M. A. McGuire, A. F. May, R. J. McQueeney, and B. C. Sales, Phys. Rev. B 100, 104409 (2019).

[23] H. Xiang, C. Lee, H.-J. Koo, X. Gong, and M.-H. Whangbo, Dalton Trans. **42**, 823 (2013).

[24] S. L. Dudarev, G. A. Botton, S. Y. Savrasov, C. J. Humphreys, and A. P. Sutton, Phys. Rev. B **57**, 1505 (1998).

[25] G. Kresse and J. Furthmüller, Comput. Mater. Sci. **6**, 15 (1996).

[26] G. Kresse and D. Joubert, Phys. Rev. B **59**, 1758 (1999).

[27] P. E. Blöchl, Phys. Rev. B **50**, 17953 (1994).

[28] J. P. Perdew, K. Burke, and M. Ernzerhof, Phys. Rev. Lett. **77**, 3865 (1996).

[29] C. Li, A. J. Freeman, H. J. F. Jansen, and C. L. Fu, Phys. Rev. B **42**, 5433 (1990).

[30] M. A. McGuire, Crystals **7**, 121 (2017).

[31] R. J. Birgeneau, W. B. Yelon, E. Cohen, and J. Makovsky, Phys. Rev. B **5**, 2607 (1972).

[32] W. B. Yelon, Oelete, and C. Vettier, J. Phys. C **8**, 2760 (1975).

[33] Y.-J. Hao, P. Liu, Y. Feng, X.-M. Ma, E. F. Schwier, M. Arita, S. Kumar, C. Hu, R. Lu, M. Zeng *et al.*, Phys. Rev. X **9**, 041038 (2019).

[34] P. Swatek, Y. Wu, L. L. Wang, K. Lee, B. Schrunk, J.-Q. Yan, and A. Kaminski, Phys. Rev. B **101**, 161109(R) (2020).